J. Fluid Mech. (2010), *vol.* 653, *pp.* 245–271.
doi:10.1017/S0022112010000376

Receptivity to free-stream vorticity of flow past a flat plate with elliptic leading edge

L.-U. SCHRADER[1], L. BRANDT[1]†, C. MAVRIPLIS[2] AND D. S. HENNINGSON[1]

[1]Linné Flow Centre, KTH Mechanics, SE-100 44 Stockholm, Sweden

[2]Department of Mechanical Engineering, University of Ottawa, Ottawa K1N 6N5 Canada

(Received 9 July 2009; revised 18 January 2010; accepted 18 January 2010; first published online 27 April 2010)

Receptivity of the two-dimensional boundary layer on a flat plate with elliptic leading edge is studied by numerical simulation. Vortical perturbations in the oncoming free stream are considered, impinging on two leading edges with different aspect ratio to identify the effect of bluntness. The relevance of the three vorticity components of natural free-stream turbulence is illuminated by considering axial, vertical and spanwise vorticity separately at different angular frequencies. The boundary layer is most receptive to zero-frequency axial vorticity, triggering a streaky pattern of alternating positive and negative streamwise disturbance velocity. This is in line with earlier numerical studies on non-modal growth of elongated structures in the Blasius boundary layer. We find that the effect of leading-edge bluntness is insignificant for axial free-stream vortices alone. On the other hand, vertical free-stream vorticity is also able to excite non-modal instability in particular at zero and low frequencies. This mechanism relies on the generation of streamwise vorticity through stretching and tilting of the vertical vortex columns at the leading edge and is significantly stronger when the leading edge is blunt. It can thus be concluded that the non-modal boundary-layer response to a free-stream turbulence field with three-dimensional vorticity is enhanced in the presence of a blunt leading edge. At high frequencies of the disturbances the boundary layer becomes receptive to spanwise free-stream vorticity, triggering Tollmien–Schlichting (T-S) modes and receptivity increases with leading-edge bluntness. The receptivity coefficients to free-stream vortices are found to be about 15 % of those to sound waves reported in the literature. For the boundary layers and free-stream perturbations considered, the amplitude of the T-S waves remains small compared with the low-frequency streak amplitudes.

1. Introduction

Numerical simulation of receptivity to free-stream vorticity of the flow over a flat plate with elliptic leading edge is considered. Receptivity denotes the process by which ambient disturbances such as sound and vorticity enter the boundary layer and initialize the formation of boundary-layer instabilities. Most numerical receptivity studies presented so far are concerned with flow over an infinitely thin flat plate downstream of the leading edge, for instance the Finite-Reynolds Number (FRNT) studies by Crouch (1992) and Choudhari & Streett (1992) (acoustic receptivity) and the

† Email address for correspondence: luca@mech.kth.se

work by Bertolotti (1997) (vortical receptivity) for Blasius flow. In contrast, Goldstein, Leib & Cowley (1992) and Goldstein & Wundrow (1998) consider through asymptotic analysis flow around a flat plate of finite thickness with an upstream vortical free-stream disturbance. Since the 1990s there have also been a smaller number of numerical simulations of flow around leading edges with different geometry, mainly dealing with acoustic receptivity. Here, we summarize the literature on acoustic and vortical leading-edge receptivity, being most relevant to our present study, and refer to the recent review by Saric, Reed & Kerschen (2002) for a complete survey.

1.1. *Leading-edge receptivity to free-stream sound*

The theoretical foundation of leading-edge receptivity to sound has been laid by Goldstein (1983) who shows through asymptotic analysis that long-wavelength acoustic free-stream disturbances are coupled to short-wavelength T-S waves via a length scale reduction mechanism near the leading edge. Goldstein, Sockol & Sanz (1983) compute receptivity coefficients, a measure for the coupling between the sound and the T-S waves, at an infinitely sharp leading edge. Heinrich & Kerschen (1989) extend this study to the case of obliquely impinging acoustic waves and find larger receptivity coefficients than those for the parallel sound waves. Receptivity to oblique sound is also investigated through asymptotic and numerical analyses by Hammerton & Kerschen (2005) for a thin cambered airfoil with parabolic leading edge. The authors show that increasing the angle-of-attack initially decreases (increases) the acoustic receptivity on the upper (lower) wing side, whereas the opposite holds when the critical angle for flow separation is approached.

Lin, Reed & Saric (1992) investigate through numerical simulation the receptivity of the boundary layer on a finite-thickness flat plate with elliptic leading edge to planar sound waves with different frequencies. They introduce the modified super-elliptic (MSE) leading edge with zero curvature at the joint to the plate, reducing undesired localized receptivity due to geometric discontinuities (see Goldstein & Hultgren 1987). The mean flow is at Reynolds number $Re_b = 2400$ with b being the plate half-thickness, and the acoustic disturbance is introduced as an unsteady free-stream boundary condition for the streamwise velocity. Considering three different leading edges Lin *et al.* (1992) find a decrease in receptivity of T-S waves to sound with increasing aspect ratio (decreasing bluntness). The juncture of the MSE leading edge, though being comparably smooth, contributes up to 50 % to the total receptivity, owing to the decay of the leading-edge induced T-S wave upstream of branch I. Fuciarelli, Reed & Lyttle (2000) present acoustic branch-I receptivity coefficients computed for the same base flow as discussed in Lin *et al.* (1992). They study the effect of angle of incidence of the sound wave and show that receptivity is more than four times as efficient at an angle of 15° as in the symmetric case. Wanderley & Corke (2001) consider two relatively sharp MSE leading edges (large aspect ratios) at $Re_b = 2400$ and study the effect of acoustic frequency. The authors show receptivity coefficients both at branch I of the T-S mode and at the leading edge. While the branch-I amplitude decreases with increasing aspect ratio, the opposite holds for the extrapolated receptivity amplitude at the leading edge. This is due to the lower adverse pressure gradient of the sharper leading edge considered, causing a faster decay of the T-S instability upstream of branch I. Wanderley & Corke (2001) also show that T-S waves excited at the juncture are superimposed on those triggered at the leading edge, which becomes apparent through local maxima and minima in the receptivity amplitude when plotted versus frequency.

1.2. *Leading-edge receptivity to vortical free-stream disturbances*

Goldstein & Leib (1993) and Wundrow & Goldstein (2001) present an asymptotic analysis of the boundary-layer response to steady low-amplitude disturbances upstream of a zero-thickness flat plate (infinitely sharp leading edge). The free-stream perturbations considered represent counter-rotating axial vortices distorting the streamwise velocity profiles via a weak cross-stream motion. This leads to steady structures of positive and negative streamwise disturbance velocities, long in streamwise and narrow in spanwise directions – similar to the Klebanoff modes (streaks) observed in flat-plate experiments with free-stream turbulence. Receptivity to axial free-stream vortices is also studied in Bertolotti & Kendall (1997). The authors report results from an experiment with a controlled axial vortex generated by a micro-wing upstream of the leading edge and compare these with numerical findings based on the parabolized stability equations (PSE). This work also shows the efficiency of axial vortices in exciting non-modal streaky instabilities in the boundary layer. The experiment was carried out on a flat plate with elliptic leading edge – the prevalent geometry in wind-tunnel testing, which highlights its relevance for theoretical and numerical studies. Goldstein *et al.* (1992) and Goldstein & Wundrow (1998) show asymptotic results for the boundary-layer response to a steady low-amplitude spanwise periodic disturbance in streamwise velocity upstream of a finite-thickness flat plate with rounded leading edge. This particular perturbation is characterized by steady vertical vorticity, with the vortex lines being stretched and tilted as the disturbance impinges on the leading edge. This mechanism first generates streamwise vorticity, which in turn produces boundary-layer streaks. Heinrich & Kerschen (1989) and Kerschen, Choudhari & Heinrich (1990) consider through an asymptotic approach the coupling between two-dimensional vortical gusts upstream of an infinitely sharp leading edge and T-S instability inside the boundary layer. Streamwise velocity disturbances are found to produce larger T-S amplitudes than those produced by vertical free-stream fluctuations.

Buter & Reed (1994) present numerical results obtained for the same configuration as presented in Lin *et al.* (1992), considering vortical high-frequency disturbances, both symmetric and asymmetric with respect to the flat-plate axis. The asymmetric perturbation, causing an oscillating forward stagnation point, leads to larger T-S wave amplitudes than that of the symmetric forcing. A linear dependence of the T-S amplitudes on the forcing magnitude is reported for both types of free-stream vorticity (linear receptivity). Both vortical disturbances cause lower receptivity amplitudes of the T-S waves than the free-stream sound presented in Lin *et al.* (1992). Buter & Reed (1994) also investigate the influence of surface curvature, using an ordinary elliptic and an MSE leading edge. Although receptivity at the juncture becomes weaker for the smoother MSE shape, the total receptivity increases due to a larger pressure-gradient maximum and an upstream shift of branch I of the T-S instability.

Here, we present results obtained by means of the Spectral Element Method (SEM) with the aim to study receptivity to free-stream vorticity of the flow over a flat plate with elliptic leading edge. Two aspects are the focus of our study: the effect of leading-edge bluntness and the relevance of the three vorticity components for receptivity. The former aspect is addressed by considering a blunt and a sharp leading edge (small and large aspect ratios); the latter by using a sufficiently simple model for free-stream vortices, enabling us to investigate the boundary-layer response to streamwise, wall-normal and spanwise free-stream vorticities separately. This is

accomplished considering vortical modes in analogy to the 'A' and 'B' modes used in Bertolotti (1997).

2. Numerical approach and flow configuration

2.1. *Numerical method*

The results are obtained using the SEM proposed by Patera (1984) to solve the three-dimensional time-dependent incompressible Navier–Stokes equations. The implementation used has been developed and described by Fischer *et al.* (2008). The physical domain is decomposed into sub-domains (spectral elements), allowing for geometric flexibility and thereby applicability to engineering problems. While sharing this flexibility with the Finite Element Method (FEM), the SEM builds on different basis functions: the local approximation of the flow field is based on high-order orthogonal polynomials. In the present implementation the Lagrange polynomial interpolants are defined on Gauss–Lobatto–Legendre (GLL) nodes. The expansion for the flow variables reads

$$\boldsymbol{u}[\boldsymbol{x}^{(l)}(r,s,t)] = \sum_{i=0}^{N}\sum_{j=0}^{N}\sum_{k=0}^{N} \hat{\boldsymbol{u}}_{ijk}^{(l)} h_i(r) h_j(s) h_k(t). \tag{2.1}$$

$\boldsymbol{x}^{(l)}$ is the mapping from the reference coordinates $(r,s,t) \in [-1,1]^3$ to the local coordinates of element l; h_i, h_j and h_k are the Nth-order Lagrange polynomials in the three local spatial directions and $\hat{\hat{u}}_{ijk}$ is the nodal spectral velocity coefficient. The order N of the polynomial basis functions is the same in the three spatial directions and usually takes values between 4 and 14. The spatial discretization is based on the weak form of the governing equations and follows the $\mathbb{P}_N - \mathbb{P}_{N-2}$ discretization by Maday & Patera (1989), i.e. the pressure grid, staggered with respect to the velocity grid, is of order $N-2$. The time integration employs a high-order operator-splitting method (Maday, Patera & Ronquist 1990; Fischer 1997), with the convective terms computed explicitly via an extrapolation method and the viscous terms treated implicitly with a third-order backward-differentiation scheme. To stabilize the simulation the solution is slightly damped at highest order (5 % reduction), allowing for a larger time step while hardly degrading the spectral accuracy (see also Fischer & Mullen 2001).

The spectral nature of the SEM ensures exponential convergence of the solution for sufficiently smooth flow fields as the resolution of the numerical domain is refined by raising N. Apart from this so-called p-refinement the SEM provides a second refinement strategy through reduction of the size (raising the number K) of the elements (h-refinement), allowing for localized and adaptive refining of the computational domain (see e.g. Feng & Mavriplis 2002). Since the computational cost of the SEM is estimated as $O(KN^4)$ for three-dimensional problems (Tufo & Fischer 1999), the two refinement strategies have a different effect on the simulation cost. The paramount benefit of the present implementation is its efficient element-wise parallelization for computations on large parallel supercomputers. Tufo & Fischer (1999) show for a simulation of roughness-generated hairpin vortices in boundary-layer flow that the speed-up of parallel computations on up to 2048 processors is nearly linear. Most of the present simulations have been carried out on 512 processors. Ohlsson *et al.* (2009) report for turbulent channel flow that the efficiency of the SEM code is about one tenth of that of their Fourier–Chebyshev pseudo-spectral code.

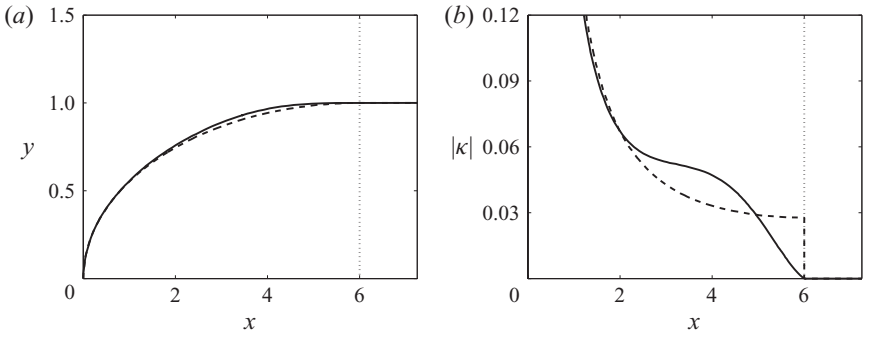

FIGURE 1. (*a*) Leading edge with aspect ratio $AR = 6$ of MSE (——) and ordinary elliptic shape (----). *y* axis enlarged. (*b*) Surface curvature of the shapes in (*a*). ···, Juncture between leading edge and flat plate.

2.2. *Base flow*

Semi-infinite flat plates with MSE leading edges are considered. The super-ellipse is defined by

$$\left(\frac{y}{b}\right)^2 = 1 - \left(\frac{a-x}{a}\right)^p, \tag{2.2}$$

where the exponent p is

$$p = 2 + \left(\frac{x}{a}\right)^2 \tag{2.3}$$

and x and y are the axial and the vertical coordinates. This type of geometry has been proposed in Lin *et al.* (1992), as it provides smoothness in curvature at the juncture to the flat plate, thus reducing undesired localized receptivity. a and b are the semi-major and -minor axes of the ellipse. The exponent p rises smoothly from 2 to 3 from the tip of the leading edge to the joint with the plate, which results in zero curvature at the joint. To identify the influence of leading-edge curvature and thus mean pressure gradient, two different leading edges are investigated, a blunt one with aspect ratio $AR \equiv a/b = 6$ and a sharp one with $AR = 20$. Figure 1(*a*) shows the MSE leading edge with $AR = 6$ in comparison with a leading edge with ordinary elliptic shape. The MSE type has a slightly fuller contour than the ordinary elliptic type; the most remarkable feature is, however, the smoothness in curvature at the juncture seen in figure 1(*b*).

Figure 2 displays the computational mesh around the leading edge with $AR = 6$. In figure 2(*a*) the elements in the upstream part of the grid are depicted, while figure 2(*b*) gives a close-up view of the nose region, also showing the GLL nodes inside the spectral elements. The parameters of the meshes used are compiled in table 1. In the upstream region the full body is meshed, which allows the introduction of asymmetric disturbances with respect to the symmetry plane of the body. A large portion of the mesh is clipped in the lower part of the domain to reduce the computational costs, i.e. only a small part of the n_{tg} elements listed in table 1 is located below the symmetry plane of the body. The base flow, independent of the spanwise direction, is computed on the two-dimensional grids.

The polynomial order is $N = 7$ in each direction. The semi-minor axis b of the elliptic leading edge, at the same time the half-thickness of the plate, is chosen as the reference length. The reference velocity is the undisturbed inflow velocity U_∞, and

	Size	$l_{ax} \times l_{vt} \times l_{sp}$	$n_{tg} \times n_{no} \times n_{sp}$	N	$N_{v,tot}$	$N_{p,tot}$
Two-dimensional	Short	224.33×45.83	150×17	7	126 120	91 800
	Medium	432.67×45.83	220×17	7	184 920	134 640
	Long	641×45.83	287×17	7	241 200	175 644
Three-dimensional	Short	$224.33 \times 45.83 \times 17.45$	$150 \times 17 \times 5$	7	4 540 320	2 754 000
	Medium	$432.67 \times 45.83 \times 17.45$	$220 \times 17 \times 5$	7	6 657 120	4 039 200

TABLE 1. Parameters of the numerical grids: size of the domain in axial, vertical and spanwise directions ($l_{ax} \times l_{vt} \times l_{sp}$), number of elements in tangential, normal and spanwise directions ($n_{tg} \times n_{no} \times n_{sp}$), order N of polynomial basis functions and total number of nodes $N_{v,tot}$ of the velocity grid and $N_{p,tot}$ of the pressure grid. Two-dimensional: $N_{v,tot} = (n_{tg}N+1)(n_{no}N+1)$ and $N_{p,tot} = n_{tg}n_{no}(N-1)^2$; three-dimensional: $N_{v,tot} = (n_{tg}N+1)(n_{no}N+1)(n_{sp}N+1)$ and $N_{p,tot} = n_{tg}n_{no}n_{sp}(N-1)^3$.

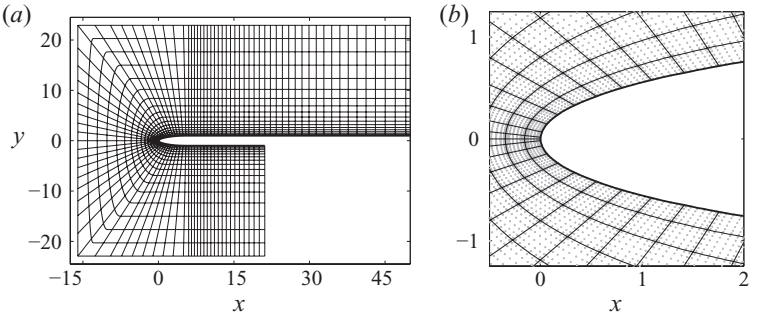

FIGURE 2. Computational grid for the blunt leading edge ($AR = 6$). (*a*) Distribution of the spectral elements in the upstream part of the body. (*b*) Close-up view of the nose region. Grey dots: Gauss–Lobatto–Legendre (GLL) points.

the kinematic viscosity is chosen such that the reference Reynolds number becomes $Re_b = U_\infty b/\nu = 2400$, as in Lin *et al.* (1992), Buter & Reed (1994) and Wanderley & Corke (2001). The outflow Reynolds number is then $Re_L = U_\infty L/\nu = 0.5/1/1.5 \times 10^6$ for the short/medium/long grid, where L is the streamwise location of the outflow plane.

No-slip conditions are prescribed on the wall. The mean-flow conditions along the far-field boundary (inflow plane and free-stream boundary) are of Dirichlet type, obtained from a potential-flow solution around a corresponding body thickened by the displacement thickness of the evolving boundary layer. The latter is estimated by combining a preliminary inviscid solution with a boundary-layer solver. This procedure allows for far-field boundaries located rather close to the plate, while the desired zero-pressure gradient along its flat part is maintained. The inflow plane is $16b$ ahead of the leading edge, where the free stream is still nearly uniform and the presence of the body is hardly felt. This is seen in figure 3 showing the far-field boundary conditions for the mean flow around the blunt leading edge ($AR = 6$). The axial velocity defect on the stagnation streamline is less than $0.02U_\infty$, and the vertical displacement velocity is about $\pm 0.01U_\infty$. The chosen position ensures a sufficiently uniform inflow while reducing the length of the upstream region and thus the computational costs. For $AR = 20$ the deviation from a uniform inflow is even smaller. The upper and lower free-stream boundaries are $23b$ (11 99 %-layer

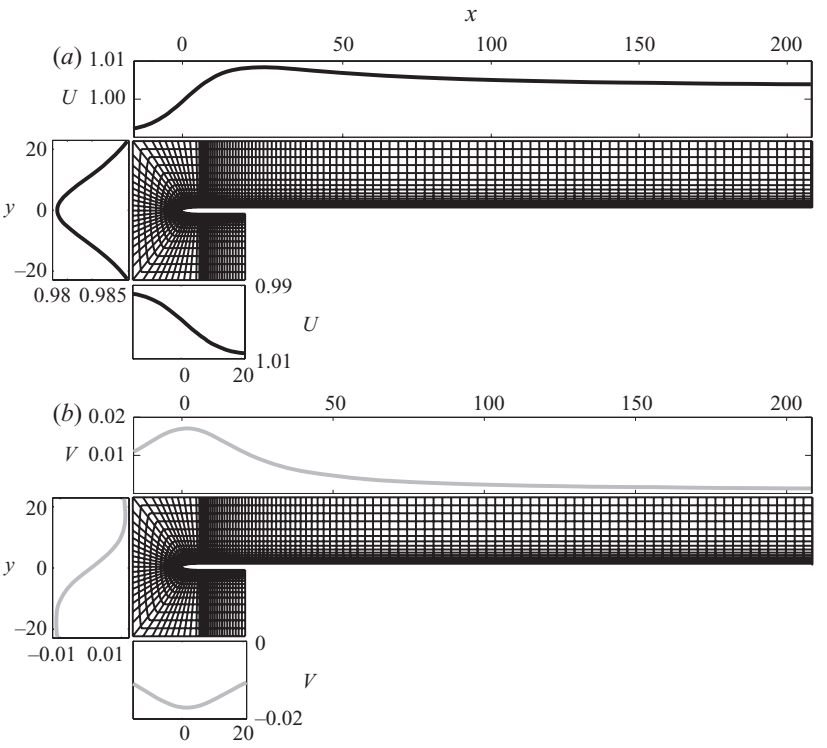

FIGURE 3. Far-field Dirichlet boundary conditions used for the mean-flow computation. Blunt leading edge ($AR = 6$). The curves are extracted from a potential-flow solution around the plate thickened by the displacement thickness. (*a*) Axial and (*b*) vertical mean velocities.

thicknesses at $Re_x = 10^6$) away from the centreline of the body. At the outflow boundaries above and below the symmetry plane von-Neumann conditions for the velocity are prescribed, while no boundary conditions are associated directly with the pressure (staggered grid). This type of outflow is found to be suitable for the low-amplitude perturbations considered, producing a smooth pressure field without spurious fluctuations.

2.3. *Perturbed flow*

The perturbed flow is computed on the three-dimensional meshes in table 1. In the spanwise direction z, five spectral elements with a total of 36 points are used, and the width of the domain is $17.45b$. The three-dimensional simulations are initialized with the spanwise extended planar base flow, and periodicity conditions are applied at the lateral domain boundaries.

2.3.1. *Vortical modes*

Fourier modes of the form $\boldsymbol{\phi} = \hat{\boldsymbol{\phi}} e^{i(\alpha x + \gamma y + \beta z - \omega t)}$ are used as a model for free-stream vorticity, where $\boldsymbol{\phi}$ is a placeholder for velocity and vorticity respectively; α, γ and β denote the axial, vertical and spanwise wavenumbers and t and ω are time and angular frequency, respectively. The axial, vertical and spanwise disturbance velocity and vorticity are denoted as (u, v, w) and (ξ, η, ζ). The amplitude functions $\hat{\boldsymbol{\phi}}$ can be derived by considering a single vorticity component, ξ say, along with the continuity

equation,

$$\mathrm{i}\hat{\xi} = \beta\hat{v} - \gamma\hat{w}, \tag{2.4a}$$

$$0 = \alpha\hat{u} + \gamma\hat{v} + \beta\hat{w}. \tag{2.4b}$$

Vorticity and velocity pointing in the same direction ($\hat{\xi}$ and $\hat{u}$ here) evolve independently of each other in a uniform stream. Therefore, without loss of generality, $\hat{u}$ is set to zero in the inflow region, and the first term on the right-hand side of (2.4*b*) is dropped. A disturbance field with one vorticity component alone is, however, sustained only in uniform flow, e.g. far upstream of a body. Figure 3 shows, though, that the mean flow is exposed to a weak irrotational distortion in the inflow region such that a small adjustment of the vortical disturbance to the underlying flow is expected.

Using (2.4), the velocity amplitudes $\hat{v}$ and $\hat{w}$ are readily expressed in terms of streamwise vorticity $\hat{\xi}$ as

$$\hat{v} = \frac{\mathrm{i}\beta}{\gamma^2+\beta^2}\hat{\xi} \quad \text{and} \quad \hat{w} = -\frac{\mathrm{i}\gamma}{\gamma^2+\beta^2}\hat{\xi}. \tag{2.5}$$

We choose $\hat{\xi} = \sqrt{\gamma^2+\beta^2}$, implying that the streamwise vorticity is proportional to the length of the wavenumber vector (γ, β) on the inflow plane. The velocity and vorticity components then read

$$(\hat{u}, \hat{v}, \hat{w}) = \frac{\mathrm{i}}{\sqrt{\gamma^2+\beta^2}}\ (0, \beta, -\gamma), \tag{2.6a}$$

$$(\hat{\xi}, \hat{\eta}, \hat{\zeta}) = \frac{1}{\sqrt{\gamma^2+\beta^2}}\ (\gamma^2+\beta^2, -\alpha\gamma, -\alpha\beta). \tag{2.6b}$$

The vortical mode is hence obtained by selecting a certain inflow wavenumber vector (γ, β) and a certain streamwise wavenumber α. Note that the magnitude of the disturbance vector $(\hat{u}, \hat{v}, \hat{w})$ does not depend on (γ, β) under the normalization adopted, i.e. the energy of the vortical mode is independent of its length scale. Note as well that the lateral vorticity components $\hat{\eta}$ and $\hat{\zeta}$ vanish when $\alpha = 0$ such that the resulting free-stream mode contains solely the streamwise vorticity.

The free-stream mode defined above is similar to the model used by Bertolotti (1997), which in turn dates back to the work of Rogler & Reshotko (1976). The formulation of Bertolotti (1997) is, however, slightly more complicated, as the vortical disturbance used there has been inserted in the free-stream above a Blasius boundary layer. Thus, the model in that work includes a streamwise decay rate and a correction due to displacement of the vortical modes by the growing boundary layer. Both effects are implicit in the numerical simulations presented here. Except for these corrections, the formulation in (2.6) is identical to mode 'B' in Bertolotti (1997); here, we adopt the notation 'ξ-mode' to emphasize the vorticity component involved in its derivation.

A vortical mode can also be derived starting from the wall-normal vorticity component η plus $v = 0$ or from spanwise vorticity ζ along with $w = 0$. Based on η, the expressions read

$$(\hat{u}, \hat{v}, \hat{w}) = \frac{\mathrm{i}}{\sqrt{\alpha^2+\beta^2}}\ (-\beta, 0, \alpha), \tag{2.7a}$$

$$(\hat{\xi}, \hat{\eta}, \hat{\zeta}) = \frac{1}{\sqrt{\alpha^2+\beta^2}}\ (-\alpha\gamma, \alpha^2+\beta^2, -\gamma\beta), \tag{2.7b}$$

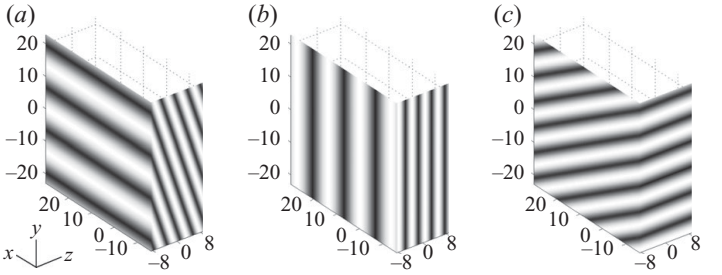

FIGURE 4. Normalized magnitude of vorticity (black: 0; white: 1). (*a*) ξ-mode with $\beta = 0.72$, $\gamma = 0.24$ and $F = 0$ (axial vorticity). (*b*) η-mode with $\beta = 0.72$, $\gamma = 0$ and $F = 96$ (vertical vorticity). (*c*) ζ-mode with $\beta = 0$, $\gamma = 0.4032$ and $F = 96$ (spanwise vorticity).

while starting from ζ yields

$$(\hat{u}, \hat{v}, \hat{w}) = \frac{\mathrm{i}}{\sqrt{\alpha^2 + \gamma^2}} \ (\gamma, -\alpha, 0), \tag{2.8a}$$

$$(\hat{\xi}, \hat{\eta}, \hat{\zeta}) = \frac{1}{\sqrt{\alpha^2 + \gamma^2}} \ (-\alpha\beta, -\gamma\beta, \alpha^2 + \gamma^2). \tag{2.8b}$$

Here, we label the mode defined in (2.7) as the 'η-mode' and that in (2.8) the 'ζ-mode'. Note that pure vertical vorticity is obtained from the η-mode, if the wall-normal wavenumber is $\gamma = 0$. In the same fashion, only the spanwise vorticity component of the ζ-mode does not vanish when the spanwise wavenumber is $\beta = 0$. The ζ-mode has also been considered in Bertolotti (1997) and is called mode 'A' there. We point out that the three modes are not linearly independent; in fact, any of the solutions 'ξ', 'η' and 'ζ' can be obtained by combining the other two types. The η-mode, for instance, can be written as a linear combination of the ξ- and ζ-modes

$$\text{`}\eta\text{'} = -\frac{1}{\gamma\sqrt{\alpha^2 + \beta^2}} \ [\beta\sqrt{\alpha^2 + \gamma^2} \cdot (\text{`}\zeta\text{'}) + \alpha\sqrt{\gamma^2 + \beta^2} \cdot (\text{`}\xi\text{'})] \tag{2.9}$$

Figure 4 displays the three types of modes in terms of the vorticity magnitude (enstrophy) in a box with y–z planes equal to the inflow plane of the computational domain. Figure 4(*a*) shows the structure of the ξ-mode with $\beta = 0.72$, $\gamma = 0.24$ and $F = 0$, figure 4(*b*) depicts the η-mode with $\beta = 0.72$, $\gamma = 0$ and $F = 96$ and figure 4(*c*) shows the ζ-mode for $\beta = 0$, $\gamma = 0.4032$ and $F = 96$. Clearly, the modes reduce to axial, vertical and spanwise vortex rolls respectively in these particular cases.

2.3.2. *Free-stream disturbance*

The response of the boundary layer to the vortical modes defined above depends on the streamwise, vertical and spanwise wavenumbers α, γ and β. A parametric study of the effect of wavenumber is outlined in the next section. To limit the number of simulations and thus the computational costs, several modes with different spanwise wavenumber are simultaneously inserted at the inflow plane. The modes are superimposed using random phase angles to ensure a total disturbance with homogeneous distribution, amenable to a characterization in terms of root mean square (r.m.s.) velocities. The total free-stream disturbance is scaled to obtain a mean inflow fluctuation amplitude $\varepsilon_{in} \ll U_\infty$, defined as

$$\varepsilon_{in} = \sqrt{\tfrac{1}{2}(\overline{u^2} + \overline{v^2} + \overline{w^2})}, \tag{2.10}$$

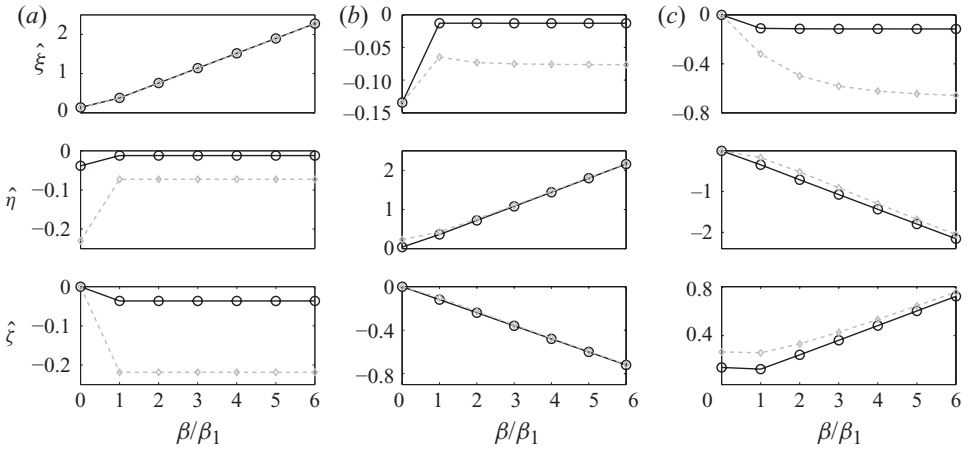

FIGURE 5. Vorticity amplitudes of inflow disturbances constructed from seven vortical modes with wavenumber $(\gamma, \beta)_0 = (0.1344, 0)$; $(\gamma, \beta)_j = (0.12, 0.36)j$, $j = 1 \ldots 6$. Frequency $F = 16$ (black ——, ○) and $F = 96$ (grey ----, ◇). (*a*) ξ-modes. (*b*) η-modes. (*c*) ζ-modes.

where the bar denotes the vertical average of the spanwise r.m.s. disturbance velocities. Note that one of the velocity components in (2.10) is always zero. A small value for ε_{in}, together with the spanwise homogeneity of the base flow, ensures that the different modes prescribed at the inlet evolve in essence independently of each other without significant nonlinear interaction. We further define a free-stream fluctuation amplitude ε_{le} at the leading edge in the same way as in (2.10). Using ε_{le} instead of ε_{in} for the normalization of disturbance amplitudes excludes the decay of the free-stream fluctuations from the inlet to the leading edge, thus ensuring independence of the results from the location of the inflow plane. On prescribing the inflow disturbance conditions the chordwise wavenumber α in (2.6)–(2.8) is substituted with the angular frequency ω via Taylor's hypothesis, assuming a phase speed $c = U_\infty = 1$ at the inlet; ω, in turn, is expressed in terms of the reduced frequency,

$$F \equiv \frac{\nu}{U_\infty^2} 10^6 \omega = \frac{L}{Re_L U_\infty} 10^6 \omega. \tag{2.11}$$

Figure 5 gives the vorticity amplitudes of three inflow disturbances constructed from vortical ξ-, η- and ζ-modes, respectively. The disturbances consist of seven modes with different wavenumbers (γ, β), chosen to match those given in Bertolotti (1997), and are plotted for low and high frequencies ($F = 16$ and 96). The free-stream fluctuations composed of ξ-modes in figure 5(*a*) are dominated by axial vortices, the amplitudes of which are independent of F; the disturbance fields based on η- and ζ-modes in figures 5(*b*) and 5(*c*) have a predominant vertical vorticity component for both frequencies. The vorticity distribution for η- and ζ-modes is in fact similar except for the sign. These three inflow perturbations are used later to investigate the receptivity of the boundary layer to free-stream vorticity.

2.4. *Validation*

A resolution study on a small test domain of the leading-edge region revealed that results obtained on an *h*- and a *p*-refined mesh ($\approx$1.5 times as many elements and $N = 9$, respectively) are in good agreement with those for the present grids. In order to validate the method described in § 2.2 to compute the Dirichlet boundary conditions for the base flow we compare the pressure distribution obtained with the present SEM

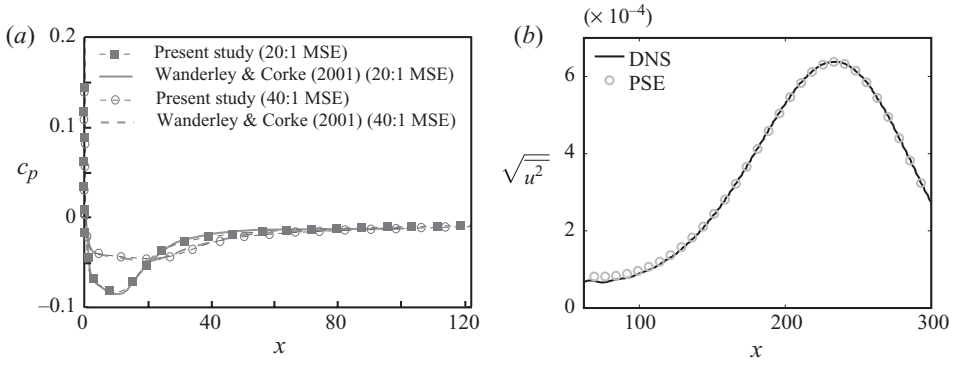

FIGURE 6. (*a*) Chordwise distribution of the pressure coefficient along a flat plate with $AR = 20$ and $AR = 40$ leading edge. Comparison with results from Wanderley & Corke (2001). (*b*) Growth and decay of T-S instability ($F = 96$) in the boundary-layer downstream of a leading edge with $AR = 6$. Results from DNS (Spectral Element Method) and PSE calculations.

code with results published in Wanderley & Corke (2001). There, MSE leading edges with $AR = 20$ and 40 are considered. Figure 6(*a*) depicts the chordwise distribution of the pressure coefficient c_p. The desired constant pressure is approached on the flat part of the plate, and good agreement between the present c_p curves and those from Wanderley & Corke (2001) is observed for both leading edges. Figure 6(*b*) shows a comparison between results obtained with the present SEM code and those from a PSE calculation. The evolution of a T-S wave with frequency $F = 96$ is considered. Good agreement in terms of streamwise r.m.s. amplitude is obtained, verifying that the grid resolution is fine enough to correctly predict the development of a short instability wave.

3. Results

3.1. *Base flow*

Figure 7 gives a characterization of the mean flow around the plates with blunt and sharp leading edges in comparison with Blasius flow. In figure 7(*a*) the pressure coefficient c_p and its chordwise derivative are plotted along the chord of the plate. The suction peak is more distinct when $AR = 6$, resulting in a stronger adverse pressure gradient than for $AR = 20$. For both leading edges, in the region $x \gtrsim 100$, c_p drops less than 1 % over a length of 100 plate half-thicknesses; for $x \gtrsim 220$, the drop in c_p is even less than 0.1 % per 100*b*. The downstream flow is thus essentially of Blasius type. Figure 7(*b*) shows the displacement thickness δ^* versus the surface coordinate s. Downstream of the junction, the δ^* distribution becomes a straight line with slope 1/2 in the double-logarithmic plot, as in Blasius flow; upstream of it δ^* increases more rapidly due to flow deceleration downstream of the pressure minimum. In figure 7(*c*) the mean wall vorticity ζ_w is displayed along s. ζ_w approaches the Blasius solution further downstream and is less smooth near the junction when $AR = 6$ – a typical behaviour on bluff bodies. Figure 7(*d*) shows that the shape factor $H_{\delta\theta}$ on the leading edges is much larger than the Blasius value of 2.59, approaching it downstream of the junction, yet remaining about 2 % larger within the computational domain.

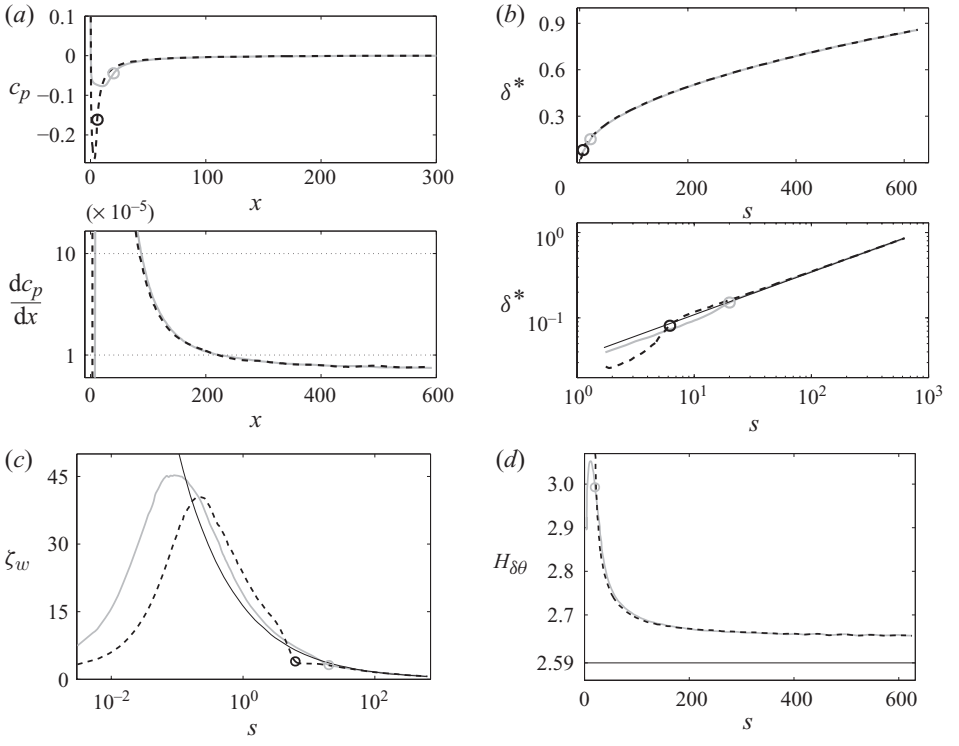

FIGURE 7. Comparison of the mean flow past the blunt (black ----, $AR = 6$) and the sharp leading edges (grey ——, $AR = 20$) with the Blasius boundary layer (——, thin). (*a*) Pressure coefficient and its streamwise derivative versus streamwise coordinate. (*b*) Displacement thickness versus surface coordinate. (*c*) Wall vorticity. (*d*) Shape factor. The circles mark the juncture.

3.2. *Perturbed flow*

3.2.1. *ξ-modes*

Figure 8 displays the boundary-layer response to low-amplitude free-stream fluctuations constructed from seven ξ-modes ($AR = 6$ leading edge). Two values of the frequency are considered: $F = 16$ and 96. This perturbation, shown in figure 5(*a*), is dominated by axial vortices, while the lateral vorticity components are smaller by one order of magnitude. The excited boundary-layer disturbance is most energetic in the axial velocity component and takes the form of streamwise elongated structures (streaks) with axial wavenumber $\alpha \sim F$. The disturbance is concentrated in different regions when F is changed: close to the wall for $F = 16$ and near the layer edge when $F = 96$. This behaviour, observed before in Blasius flow (e.g. Zaki & Saha 2009), is associated with the penetration of the free-stream modes into the shear region, being larger at low frequency. Figure 8(*b*) shows the spanwise r.m.s. of the streamwise disturbance, normalized by the amplitude ε_{le} of the free-stream fluctuations. The low-frequency streaks due to ξ-modes with $F = 16$ amplify in the region $x \lesssim 100$ ($Re_x \lesssim 2.4 \times 10^5$) and attain a significant streamwise r.m.s. amplitude before decaying. The vortical modes with high frequency ($F = 96$) are also able to enter the shear layer at the leading edge, but the excited disturbance is damped inside it. Since the high-frequency vortical disturbance is associated with a shorter streamwise length scale than that with low frequency, this result indicates that the boundary layer is

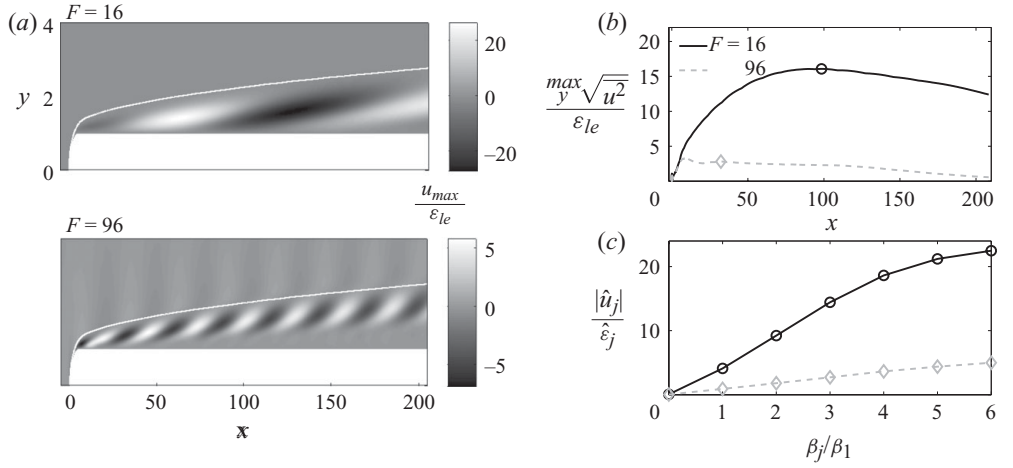

FIGURE 8. Boundary-layer response to ξ-modes with frequencies $F = 16$ and $F = 96$. Free-stream disturbance consisting of seven modes with $(\gamma, \beta)_0 = (0.1344, 0)$; $(\gamma, \beta)_j = (0.12, 0.36)j$, $j = 1 \ldots 6$; amplitude $\varepsilon_{in} = 10^{-5}$. Leading edge with $AR = 6$. (*a*) x–y plane of normalized streamwise disturbance (maximum value in y, z). Wall-normal coordinate stretched; lines mark δ_{99}. (*b*) Normalized spanwise r.m.s. of u. (*c*) Spanwise-wavenumber spectrum at the location marked by the symbol in (*b*).

more receptive to long vortical waves. Figure 8(*c*) depicts the spanwise-wavenumber spectrum of the boundary-layer disturbance. The spanwise Fourier transforms are extracted downstream of the junction, where the r.m.s. amplitudes in figure 8(*b*) are maximum, and they are normalized by the spectral amplitude $\hat{\varepsilon}_j$ of their counterparts in the oncoming free-stream disturbance. $\hat{\varepsilon}_j$ is defined in analogy to (2.10)

$$\hat{\varepsilon}_j = \sqrt{\tfrac{1}{2}(|\hat{u}_j|^2 + |\hat{v}_j|^2 + |\hat{w}_j|^2)}, \tag{3.1}$$

with $\hat{u}_j$, $\hat{v}_j$ and $\hat{w}_j$ being the velocity Fourier coefficients of the jth free-stream mode at the leading edge. For both frequencies the boundary layer is most receptive at the scale $\beta_6 = 2.16$; however, streaks with spanwise wavenumber $\beta > \beta_6$ may attain even higher amplitudes. In Schrader (2008) the largest amplitude has indeed been found for streaks with $\beta = 2.88$, translating into a streak spacing comparable to the 99 % boundary-layer thickness at $Re_x = 10^6$.

Axial free-stream vorticity

Figure 8 suggests that boundary-layer receptivity increases with decreasing forcing frequency; ξ-modes with zero frequency are thus expected to trigger a particularly strong boundary-layer response. $F = 0$ defines a special set of ξ-modes with one-dimensional vorticity vector pointing in the streamwise direction. We denote these modes 'ξ_x-modes' to emphasize their purely axial vorticity and use them to identify the role of streamwise vortices for boundary-layer receptivity. The inflow wavenumbers are $(\gamma, \beta)_j = (0.12, 0.36)j$, $j = 1 \ldots 6$. These values match those used in the PSE study by Bertolotti (1997); in particular, the modes $j = 2$ and $j = 4$ correspond to the $\beta = 0.09$ and the $\beta = 0.18$ mode of Bertolotti (1997, figure 6). The shortest spanwise wavelength is then about 1.4 times, and the longest about 8.4 times, the 99 %-thickness at $Re_x = 10^6$. Note that the ratio between vertical and spanwise length scale is fixed at a value of 3 for all modes included, i.e. the vortices have a different size

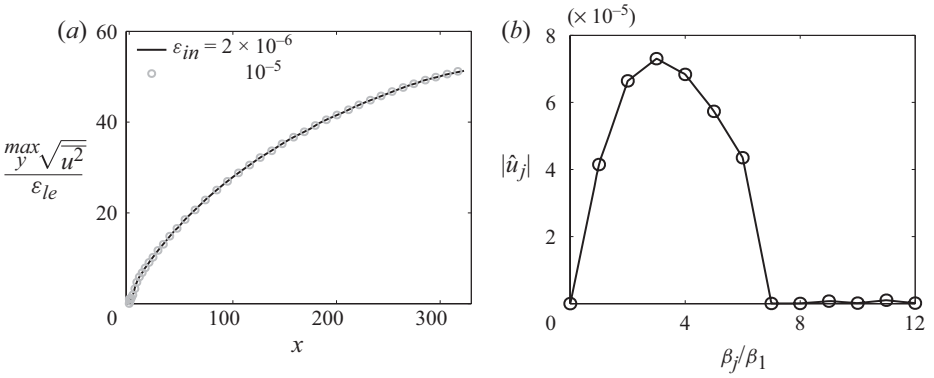

FIGURE 9. Boundary-layer disturbance excited by ξ_x-modes ($(\gamma, \beta)_j = (0.12, 0.36)j$, $j = 1 \ldots 6$) with amplitude ε_{in}. (*a*) Normalized r.m.s. of streamwise disturbance velocity for $\varepsilon_{in} = 2 \times 10^{-6}$ and 10^{-5}. (*b*) Spanwise wavenumber spectrum at $Re_x = 10^6$ when $\varepsilon_{in} = 2 \times 10^{-6}$.

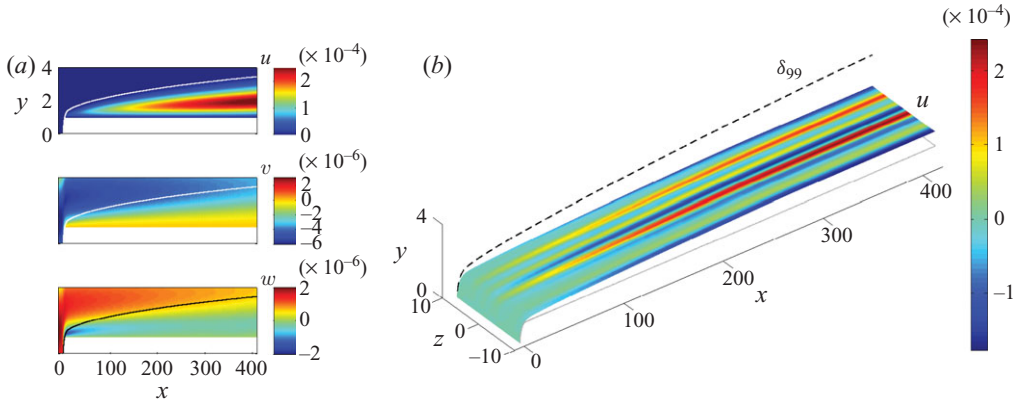

FIGURE 10. Boundary-layer response to axial free-stream vortices ($F = 0$) with $(\gamma, \beta)_j = (0.12, 0.36)\, j$, $(j = 1 \ldots 6)$ and $\varepsilon_{in} = 2 \times 10^{-6}$. Leading edge with aspect ratio $AR = 6$. (*a*) x–y plane showing the instantaneous disturbances u, v and w where u is maximum. The lines mark δ_{99}. (*b*) Spanwise plane of u along the wall-normal maximum of u_{rms}.

but the same 'proportions'. The inflow amplitude of the free-stream perturbation is $\varepsilon_{in} = 2 \times 10^{-6}$, small enough to ensure linearity in ε_{in} and to limit nonlinear interaction between modes of different length scale. Figure 9(*a*) displays the spanwise r.m.s. of streamwise velocity of the boundary-layer response to forcing with amplitude $\varepsilon_{in} = 2 \times 10^{-6}$ and a value five times larger. The normalized data collapse, that is, the flow response is linear in ε_{in} for the amplitudes considered. Figure 9(*b*) shows the spanwise-wavenumber spectrum far downstream. Modes with $\beta > \beta_6$, potentially excited by nonlinear interaction, are virtually not present in the shear layer.

Figure 10 shows the structure of the boundary-layer perturbation due to ξ_x-modes. In figure 10(*a*) the instantaneous disturbance velocities u, v and w are shown on the x–y plane of maximum u ($AR = 6$ leading edge): the perturbation has zero streamwise wavenumber and is clearly concentrated on u. Figure 10(*b*) depicts a streamwise–spanwise plane of u along the wall-normal maximum in u_{rms}. This view highlights the

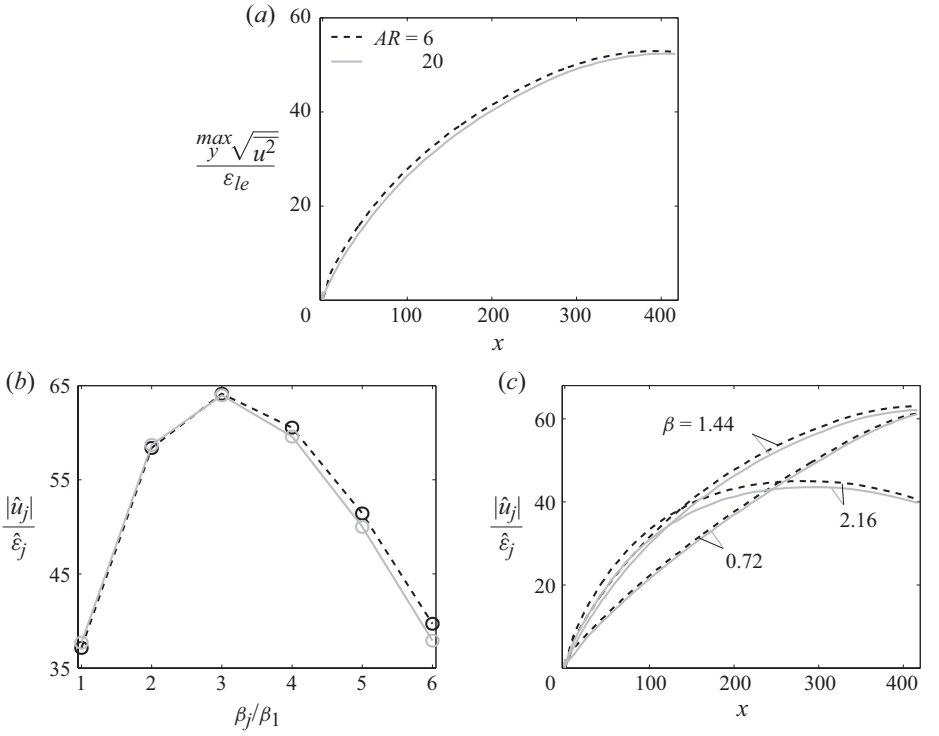

FIGURE 11. Boundary-layer response to axial free-stream vortices ($F = 0$) with $(\gamma, \beta)_j = (0.12, 0.36)j$ $(j = 1 \ldots 6)$ and $\varepsilon_{in} = 2 \times 10^{-6}$. Leading-edge aspect ratio $AR = 6$ (black ----) and 20 (grey ——). (*a*) Wall-normal maximum of normalized u_{rms}. (*b*) Spanwise wavenumber spectrum at $Re_x = 10^6$ of the boundary-layer disturbance. The modes are normalized by their free-stream values at the leading edge. (*c*) Streamwise evolution of individual normalized contributions with $\beta_2 = 0.72$, $\beta_4 = 1.44$ and $\beta_6 = 2.16$.

streaky pattern of the disturbance triggered by the steady axial free-stream vortices. These structures resemble the Klebanoff modes seen in many wind-tunnel experiments with free-stream turbulence due to upwelling and downwelling of fluid by weak vertical perturbation velocity (lift-up mechanism). This vertical motion originates from the steady free-stream vortices, capable of penetrating to some extent into the shear layer. The efficiency of steady axial vortices in generating boundary-layer streaks has also been reported (e.g. in Bertolotti 1997 and Bertolotti & Kendall 1997).

The results from figure 10 are quantified in figure 11. Both leading edges, $AR = 6$ and 20, are considered now. Figure 11(*a*) shows the wall-normal maximum of u_{rms}, normalized by the amplitude ε_{le} of the free-stream disturbance. Compared with figure 8(*b*) for $F = 16$ and 96 the steady free-stream vortices excite a boundary-layer disturbance with significantly higher downstream amplitude (more than 50 times the forcing amplitude), amplifying throughout the domain. There is little difference in u_{rms} when the $AR = 6$ leading edge is replaced by $AR = 20$. Hence, in the presence of axial free-stream vorticity, the growth of steady streaks is hardly affected by leading-edge bluntness. This behaviour has in fact been predicted by Wundrow & Goldstein (2001) through asymptotic analysis. The spectrum of spanwise wavenumbers of the downstream boundary-layer perturbation, indicating the dominant spanwise length scales, is plotted in figure 11(*b*). To quantify the receptivity of the individual spanwise

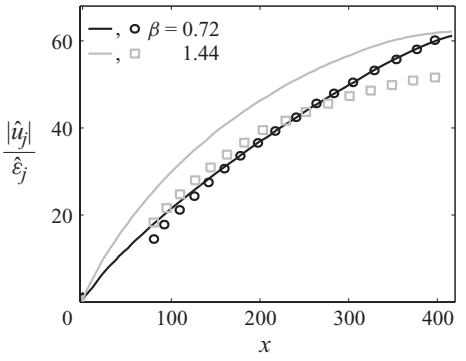

FIGURE 12. Streamwise evolution of two individual normalized modes $\beta_2 = 0.72$ (black) and $\beta_4 = 1.44$ (grey) in comparison with PSE results from Bertolotti (1997, figure 6): $\beta = 0.09$ (black circles; β_2 in our scaling); $\beta = 0.18$ (grey squares; β_4 here).

waves, the spectrum is normalized by the spectral amplitude $\hat{\varepsilon}_j$ of the corresponding scales in the free-stream. The picture is similar for both leading edges, with the amplitude peak found at $\beta_3 = 1.08$. The contributions with values of $\beta > \beta_3$ are slightly more enhanced on the leading edge with $AR = 6$. The streamwise amplification of three individual normalized disturbance components is shown in figure 11(*c*). Figure 11(*c*) also illustrates that the dominant spanwise length scale successively increases in the downstream direction with the boundary-layer thickness: near the leading edge, the shortest wave ($\beta_6 = 2.16$) dominates; at the outlet, the longest wave ($\beta_2 = 0.72$) grows the fastest. Leading-edge bluntness effects – in general small – are most pronounced for modes with short spanwise wavelength.

In figure 12 the modal evolution for $\beta_2 = 0.72$ and $\beta_4 = 1.44$ from figure 11(*c*) is compared with PSE results for Blasius flow reported in Bertolotti (1997, figure 6). The PSE data have been matched with the present curves to give good agreement for the β_2-streak in the downstream region, where the leading-edge flow has relaxed towards the Blasius solution. The evolution of this scale has been validated in Bertolotti (1997) with experimental results and is therefore considered particularly reliable. Indeed, good agreement is found for $x \gtrsim 150$ ($Re_x \gtrsim 3.6 \times 10^5$). Bertolotti (1997) also reports the evolution of the β_4-mode, forced in the PSE analysis with the same initial amplitude as the β_2-mode. The downstream growth rate of the β_4-streak is in reasonable agreement with our Direct Numerical Simulation (DNS) data whereas the amplitude level is considerably higher in our study, which we attribute to additional receptivity downstream of the leading edge and upstream of the region captured by the model in Bertolotti (1997). This suggests that leading-edge bluntness enhances receptivity to disturbances of shorter spanwise scale.

3.2.2. *η-modes*

The oncoming vortical disturbance now consists of seven low-amplitude η-modes with the same wavenumbers and frequencies as considered in § 3.2.1. This free-stream perturbation, plotted in figure 5(*b*), is made up of vortices with strong vertical and weak spanwise vorticity, while the axial component is negligible. The response of the boundary layer is illustrated in figure 13(*a*) for the leading edge with $AR = 6$, showing a streaky pattern of non-modal instability. However, the streak amplitudes seen in figure 13(*b*) are considerably lower than those in the presence of ξ-modes. Again, the low-frequency streaks attain larger r.m.s. amplitudes than those with

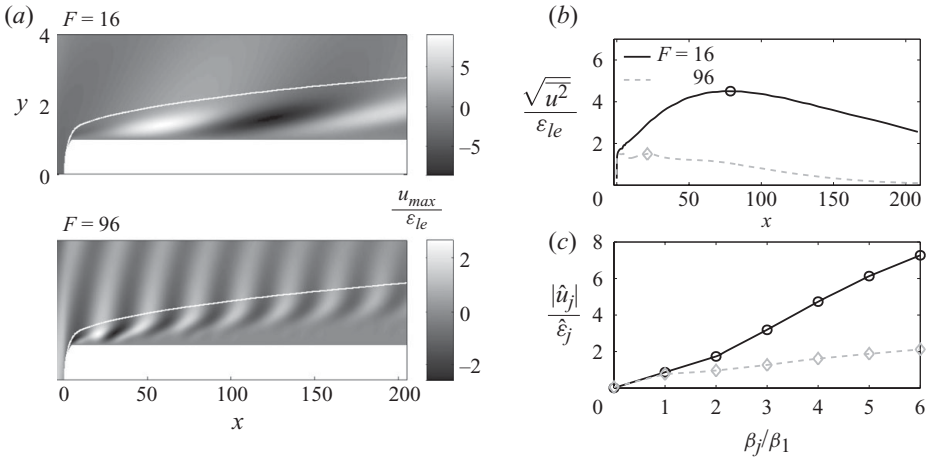

FIGURE 13. Boundary-layer response to η-modes with frequencies $F = 16$ and $F = 96$. Free-stream disturbance consisting of seven modes with $(\gamma, \beta)_0 = (0.1344, 0)$; $(\gamma, \beta)_j = (0.12, 0.36)j$, $j = 1 \ldots 6$; amplitude $\varepsilon_{in} = 10^{-5}$. Leading edge with $AR = 6$. (*a*) x–y plane of normalized streamwise disturbance (maximum value in y and z). Wall-normal coordinate stretched; lines mark δ_{99}. (*b*) Normalized spanwise r.m.s. of u. (*c*) Spanwise wavenumber spectrum at the location marked in (*b*) by the symbol.

high frequency. Figure 13(*c*) shows that the streaks with smallest spanwise length scale attain the largest amplitude for both values of F before the boundary-layer perturbation eventually decays on all scales.

Vertical free-stream vorticity

A special subset of η-modes, characterized by the absence of the axial and spanwise vorticity component, is obtained when setting the wall-normal wavenumber γ of all modes to zero. These modes, denoted by η_y-modes here, are used to establish the receptivity of the boundary layer to vertical free-stream vorticity, considering now both leading edges ($AR = 6$ and 20). The spanwise wavenumbers are $\beta_j = 0.36j$ ($j = 1 \ldots 6$), as before. The results in § 3.2.1 suggest a particularly strong flow response for free-stream fluctuations with zero frequency; in that case a vortical free-stream disturbance with only η and $u \neq 0$ is obtained. The flow response to this kind of forcing is illustrated in figure 14. The boundary layer develops steady streaks with zero streamwise wavenumber, which are qualitatively similar to the response to axial free-stream vorticity (ξ_x-modes) shown in figure 10; the disturbance amplitudes remain, however, smaller. It is concluded that the layer is also receptive to vertical free-stream vorticity with $F = 0$.

The details of the receptivity mechanism are illustrated in figure 15, displaying a spanwise extract of the disturbance field in the leading-edge region ($AR = 6$). We show, as an example, the contribution with wavenumber $(\gamma, \beta) = (0, 1.8)$ in this figure; the results for other wavenumbers and for the total disturbance are qualitatively the same. The free-stream perturbation upstream of the leading edge is manifested in an oscillating u-component while w is nearly zero and $v = 0$ per construction. When the η_y-mode impinges on the leading edge, however, a strong spanwise disturbance is produced (plane I in the figure). This is confirmed in figure 16(*a*) for the total free-stream disturbance, where the plot at the top shows in terms of spanwise r.m.s.-values that w is generated at the expense of u. This 'cross-flow' has been predicted in

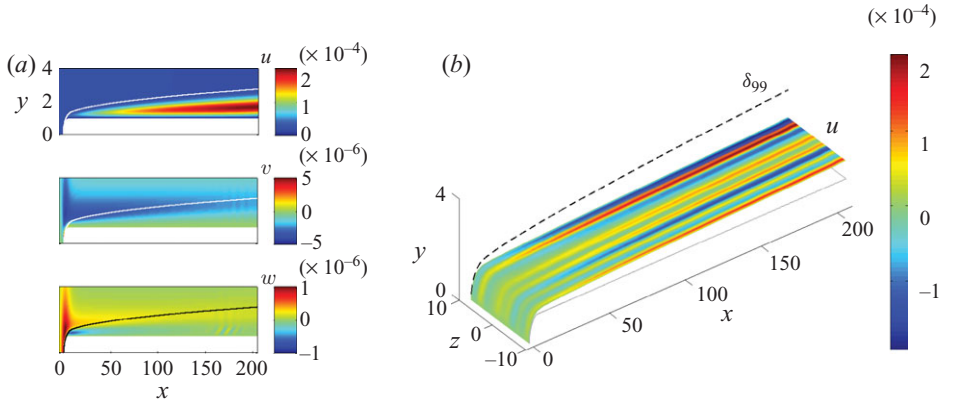

FIGURE 14. Boundary-layer response to free-stream η_y-modes (vertical vorticity) with $(\gamma, \beta)_j = (0, 0.36)j$, $j = 1 \ldots 6$; $F = 0$ and $\varepsilon_{in} = 10^{-5}$. $AR = 6$ leading edge. (*a*) x–y plane showing the instantaneous disturbances u, v and w where u is maximum. The thin lines mark δ_{99}. (*b*) Spanwise plane of u along the wall-normal maximum of u_{rms}.

Goldstein *et al.* (1992) and Goldstein & Wundrow (1998) through asymptotic analysis for the same type of upstream disturbance. Plane II in figure 15 illustrates that there is also a weak vertical motion in the boundary layer. v together with w establishes an axially oriented, counter-rotating vortical motion (see plane III of figure 15), producing the u-disturbance (streaks) in figure 14(*b*) through the lift-up mechanism. The axial vortices are active throughout the boundary layer (figure 16*b*) such that the downstream amplitude of the streaks becomes large. Figure 16 also illustrates that down-/up-washing of fluid by the vortices produces a high-/low-speed streak. The conversion of upstream vertical vorticity into downstream axial vorticity by the leading edge is limited to the region near the boundary layer. This is seen in the lower plot of figure 16(*a*): the vertical vorticity far above the plate ($y = 15b$) is nearly unaffected; v and w essentially remain zero, while u decays slowly. The vortex lines thus change orientation from the boundary layer (axial) to the free-stream (vertical), with vortex stretching and tilting being the underlying mechanisms. Goldstein *et al.* (1992) and Goldstein & Wundrow (1998) have predicted this behaviour in their asymptotic analysis.

The physical mechanism described above relies on the leading edge; bluntness effects are therefore expected to be relevant. This is highlighted in figure 17. According to figure 17(*a*) bluntness clearly enhances the disturbance magnitude, with the r.m.s. amplitude observed downstream of the $AR = 6$ leading edge being nearly three times that in the case of $AR = 20$. This is in contrast to the response to axial free-stream vortices, for which the dependence on nose bluntness is marginal. The explanation for this behaviour is illustrative in the light of figure 15: the blunt leading edge causes a stronger deformation of the oncoming η_y-modes, enhancing vortex stretching and tilting in the downstream direction. Figure 17(*a*) also indicates that the shear-layer disturbance for $F = 0$ becomes about twice as strong as that due to vertical-vorticity modes with $F = 16$ (cf. figure 13*b*); moreover growth of streaks is observed throughout the domain. This accentuates again the relevance of the steady part of vortical free-stream fluctuations. Figure 17(*b*) shows the normalized spanwise-wavenumber spectrum at $Re_x = 5 \times 10^5$. The Fourier spectrum forced by axial free-stream vorticity

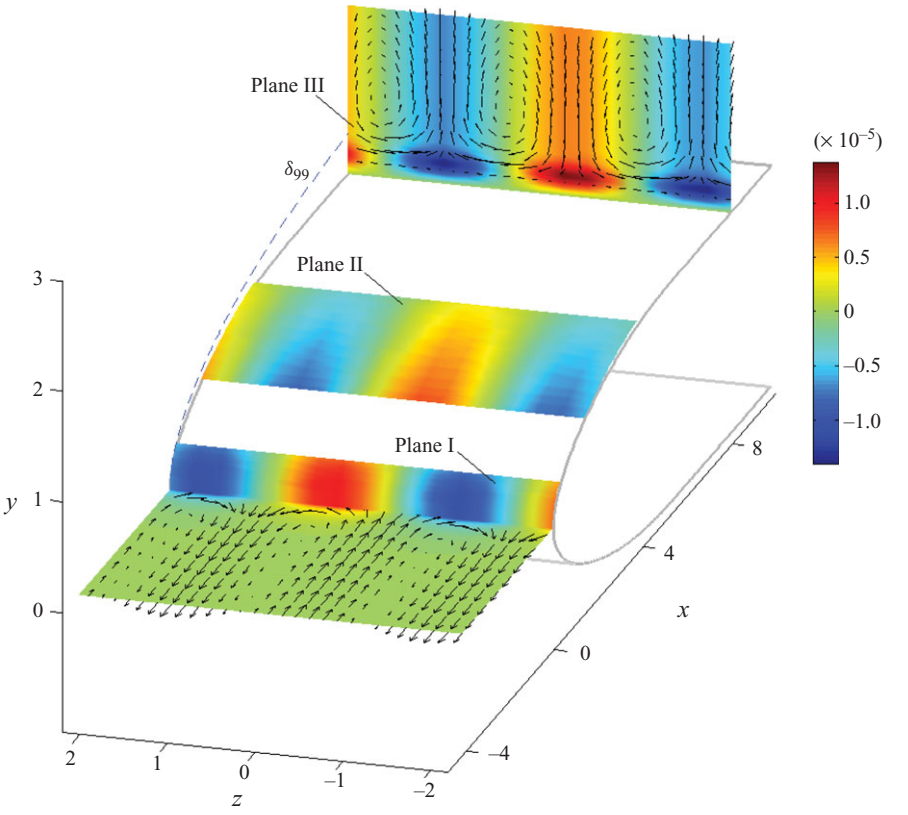

FIGURE 15. Instantaneous boundary-layer response to a single η_y-mode (vertical vorticity) with $(\gamma, \beta) = (0, 1.8)$, $F = 0$ and $\varepsilon_{in} = 10^{-5}$. Leading-edge with $AR = 6$; $\sim 1/4$ of the spanwise domain width is shown. Plane I: w (colours), u and w (vectors); plane II: $5 \cdot v$; plane III: u (colours), v and w (vectors).

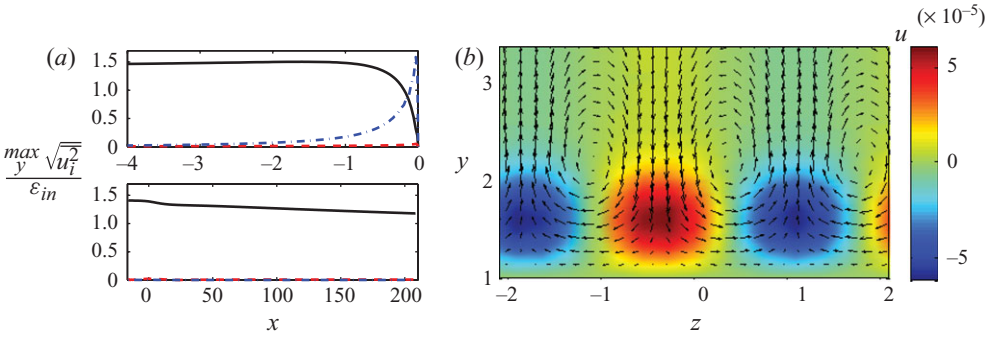

FIGURE 16. (*a*) Normalized spanwise r.m.s. of u (——), v (----) and w (-·-·-) on the stagnation streamline (top) and far above the plate ($y = 15b$, bottom) for free-stream η_y-modes with $(\gamma, \beta)_j = (0, 0.36)j$ $(j = 1 \ldots 6)$ and $F = 0$. (*b*) Instantaneous u (colours), v and w (vectors) in the boundary layer at $x = 175b$ ($Re_x = 4.2 \times 10^5$) for forcing with the η_y-mode from figure 15.

(ξ_x-modes) is shown as well for comparison (scaled by 1/5), indicating that the preferred spanwise scales due to η_y-modes are found at higher values of β than in the presence of ξ_x-modes. This suggests that the conversion of vertical into axial vorticity is more efficient for larger spanwise wavenumbers, that is, smaller vortical

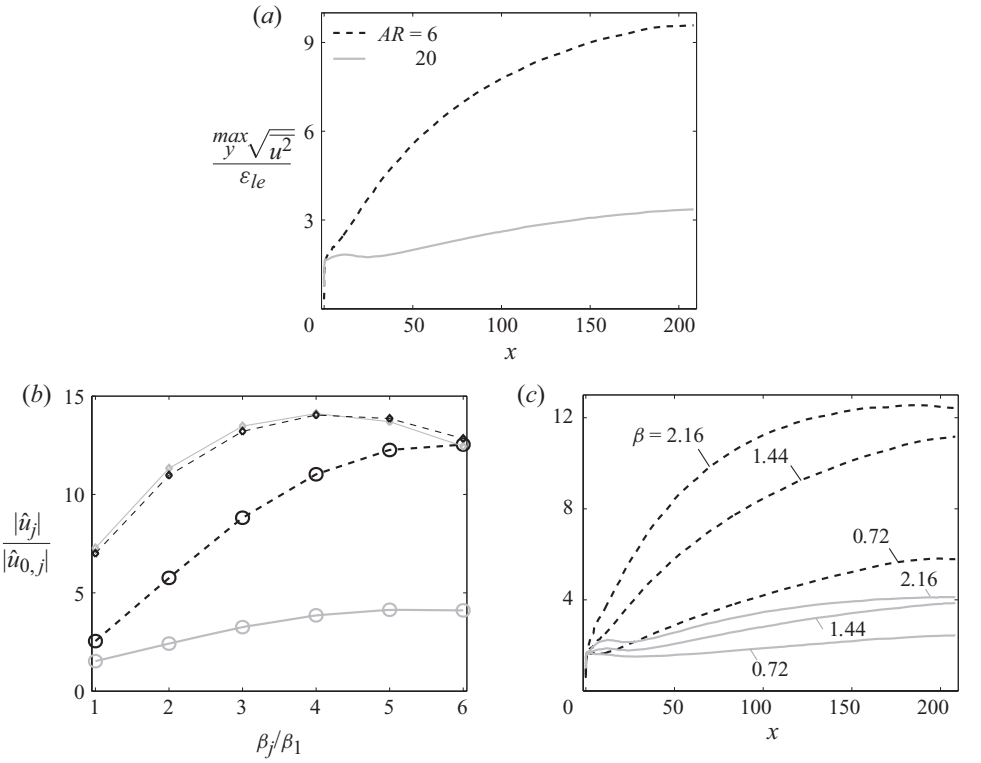

FIGURE 17. Boundary-layer response to free-stream η_y-modes (vertical vorticity) with $(\gamma, \beta)_j = (0, 0.36)j$, $j = 1 \ldots 6$; $F = 0$ and $\varepsilon_{in} = 10^{-5}$. Leading-edge aspect ratio $AR = 6$ (black) and 20 (grey). (*a*)–(*c*) as in figure 11, see there for further explanation. The β-spectrum in (*b*) is extracted at $Re_x = 5 \times 10^5$; the corresponding spectrum due to axial free-stream vortices (ξ_x-modes) is shown as well (thin lines, small symbols; scaled by factor 1/5).

structures are more easily stretched and tilted at the leading edge than larger ones. Figure 17(*c*) depicts the evolution of the streaks with wavenumber $\beta_2 = 0.72$, $\beta_4 = 1.44$ and $\beta_6 = 2.16$. The strongest downstream amplification rate is no longer seen for β_2, in contrast to the case of ξ_x-modes, but for β_4. The β_6-streaks attain the largest downstream amplitude.

To summarize, (i) there is no 'direct' receptivity to vertical free-stream vortices; the vertical vorticity component has first to be converted into streamwise vorticity. This conversion is most efficient at a blunt leading edge. (ii) Though the streak amplitude due to vertical-vorticity modes is lower than that caused by axial vortices (ratio $\approx 1/5$ for the $AR = 6$ leading edge), it is significant for sufficient leading-edge bluntness. We thus expect that the vertical vorticity component of natural three-dimensional turbulence will significantly contribute to the total boundary-layer response.

3.2.3. *ζ-modes*

The ζ-modes illustrated in figure 5(*c*) are now used to perturb the inflow. These modes have a similar vorticity distribution as the η-modes used in § 3.2.2 (except for the sign), i.e. they are also dominated by vertical vorticity. The axial vorticity component of the modes $j > 0$ is, however, somewhat stronger than that of the η-modes, and mode $j = 0$ carries spanwise vorticity instead of axial vorticity. The

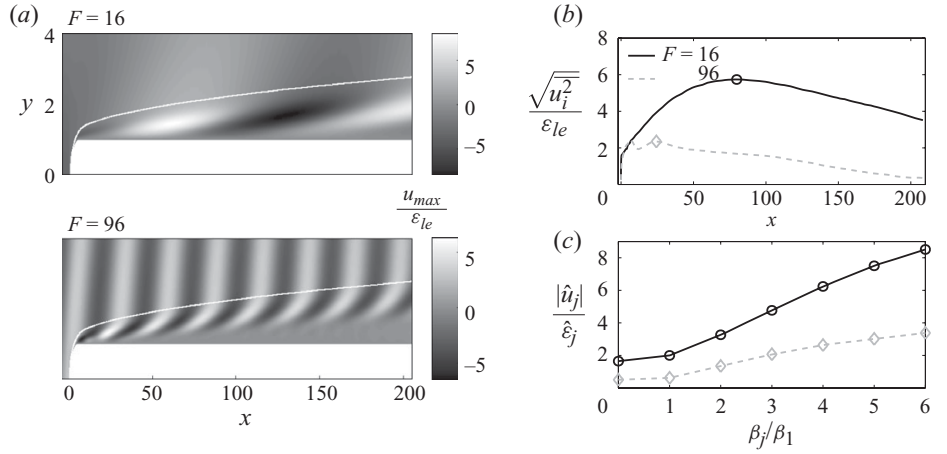

FIGURE 18. Boundary-layer response to ζ-modes with frequencies $F=16$ and $F=96$. Free-stream disturbance consisting of seven modes with $(\gamma,\beta)_0=(0.1344,0)$; $(\gamma,\beta)_j=(0.12,0.36)j$, $j=1\ldots6$; $\varepsilon_{in}=10^{-5}$. Leading edge with $AR=6$. (*a*) x–y plane of normalized streamwise disturbance (maximum value in y, z). Vertical coordinate stretched; lines mark δ_{99}. (*b*) Normalized spanwise r.m.s. of u. (*c*) Spanwise-wavenumber spectrum at the location marked in (*b*) by the symbol.

flow response, shown in figure 18, is indeed similar to that triggered by the η-modes. The r.m.s. amplitude of the streaks is, though, larger, which is attributed to the stronger axial vorticity component of the ζ-modes. Figure 18(*c*) shows that the component $\beta=0$ is also present in the excited shear-layer disturbance. This component has not been seen before when ξ- and η-modes interact with the boundary layer. The role of the $\beta=0$-contribution is addressed below.

Spanwise free-stream vorticity

Free-stream fluctuations with pure spanwise vorticity are obtained from ζ-modes with $\beta=0$ (labelled ζ_z-modes here). In this case, the vortical disturbance no longer depends on the spanwise coordinate, i.e. two-dimensional simulations similar to those in Buter & Reed (1994) can be performed. The two-dimensional grids in table 1 (medium and long) have been used (outflow Reynolds numbers 10^6 and 1.5×10^6, respectively). The amplitude of the free-stream disturbance is set to $\varepsilon_{in}=2\times10^{-3}$. The effect of frequency F and vertical wavenumber γ is investigated for both leading edges, $AR=6$ and 20. Figure 19 shows planes of streamwise and vertical disturbance velocity due to a ζ_z-mode with vertical wavenumber $\gamma=0.1344$ for (*a*) $F=96$ and (*b*) $F=56$ (leading edge $AR=6$). Stability theory for Blasius flow reveals that T-S instability can exist at these frequencies (see also Wanderley & Corke 2001). Indeed, T-S waves are identified in the boundary layer; they are, however, much weaker than the streaky disturbances excited through axial and vertical free-stream vorticity. As predicted by classic theory the unstable region is shifted downstream when the frequency is lowered from $F=96$ to 56, the T-S wave becomes longer and its amplitude smaller. Figure 19 also illustrates the difference in wavelength between the free-stream modes and the T-S waves, associated with their different propagation speed. In fact, 'wavelength reduction' is an integral part of receptivity to external disturbances, coupling the free-stream waves with the shear-layer modes (Goldstein 1983). This process takes place in the rapidly diverging part of the boundary layer near the leading edge and establishes wavenumber coupling between the vortical free-stream mode and the T-S wave.

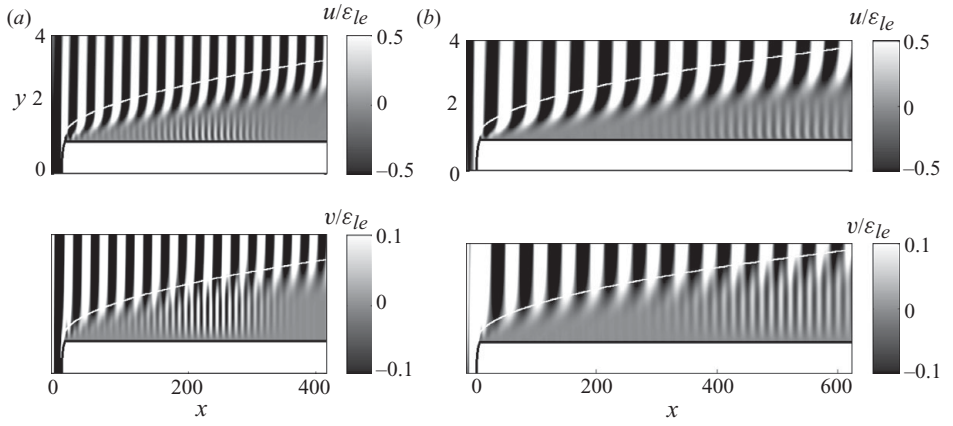

FIGURE 19. Boundary-layer response to spanwise free-stream vorticity ($\beta = 0$) with $\gamma = 56$ and $\varepsilon_{in} = 2 \times 10^{-3}$. x–y plane of u (top) and v (bottom), normalized by ε_{le}. Leading edge with $AR = 6$. (*a*) $F = 96$. (*b*) $F = 56$.

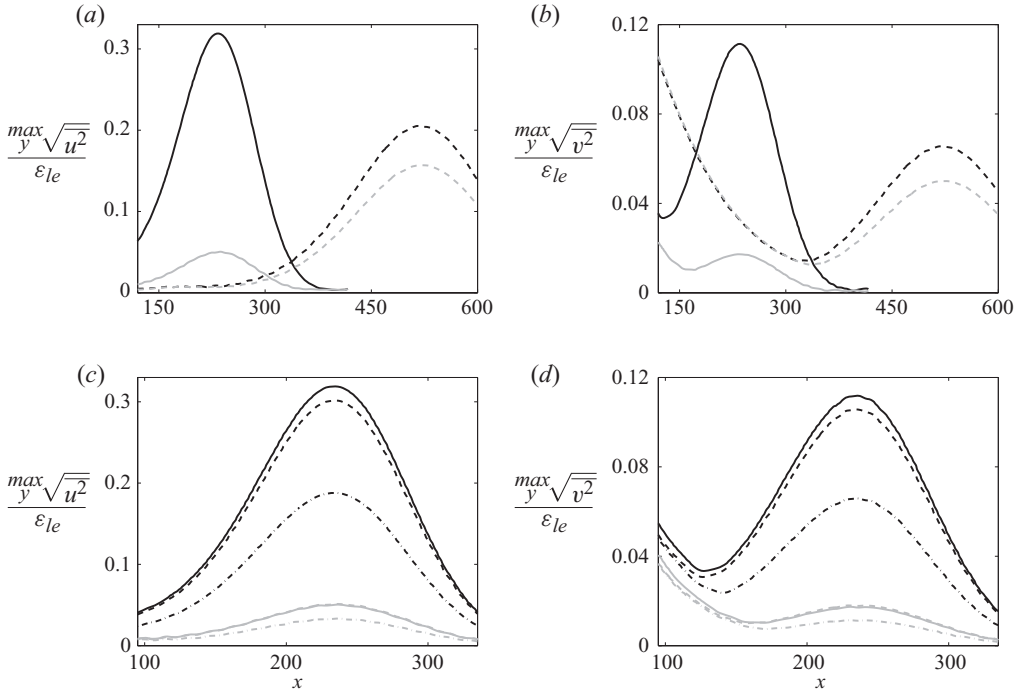

FIGURE 20. Boundary-layer response to ζ_z-modes (spanwise vorticity, $\beta = 0$) with $\varepsilon_{in} = 2 \times 10^{-3}$. Leading-edge aspect ratio $AR = 6$ (black) and 20 (grey). Normalized temporal r.m.s. of (*a*) u and (*b*) v for ζ_z-modes with $\gamma = 56$; $F = 96$ (——) and 56 (----). Normalized temporal r.m.s. of (*c*) u and (*d*) v for ζ_z-modes with $F = 96$; $\gamma = 42$ (----), 56 (——) and 168 (-·-·-).

In figure 20 the wall-normal maximum of u_{rms} and v_{rms} in the shear layer is plotted versus the chordwise coordinate (temporal r.m.s.). In figures 20(*a*) and 20(*b*) the focus is on the effect of frequency ($F = 56$ and 96) while the vertical wavenumber is fixed at $\gamma = 0.1344$; figures 20(*c*) and 20(*d*) illustrate the influence of γ on the T-S amplitudes, with F kept at 96. The effect of leading-edge shape is captured in all four figures.

The largest T-S amplitude is obtained for $F = 96$, increasing by a factor of nearly 6 when the $AR = 20$ leading edge is replaced by $AR = 6$. Hence, leading-edge bluntness drastically enhances receptivity to spanwise vortical modes with $F = 96$, whereas a change of bluntness has a less significant effect on u_{rms} and v_{rms} (factor $\approx 4/3$) when $F = 56$. The leading edges are then shorter (blunter) relative to the wavelength of the ζ_z-mode and the T-S wave, i.e. even the $AR = 20$ leading edge may be 'blunt enough' at low frequency to support efficient wavelength conversion. Figure 20(*b*) shows that the initial vertical disturbance v due to displacement of the vortical modes in the leading-edge region rapidly decays before v is generated again through the T-S mechanism. The influence of wall-normal wavenumber is shown in figures 20(*c*) and 20(*d*). Values of $\gamma = 0.1008$, 0.1344 and 0.4032 are considered. The wall-normal scale of the ζ_z-modes is then 7.5, 22.5 and 30 times the 99 %-thickness at $Re_x = 10^6$. The plots reveal that receptivity to large-scale spanwise vortical modes is more efficient than to modes with a smaller vertical scale. The highest amplitude in u_{rms} and v_{rms} is found for $\gamma = 0.1344$ in agreement with results by Bertolotti (1997) for Blasius flow. Both increasing and decreasing γ leads to a reduction of the T-S amplitudes. The relative differences in disturbance level are smaller when the leading edge is slender ($AR = 20$); in particular, the T-S amplitudes observed for $\gamma = 0.1008$ and 0.1344 are indistinguishable in the figure.

In order to quantify the efficiency of the receptivity mechanism to spanwise free-stream vorticity, receptivity coefficients are computed, defined by

$$C_I = \frac{A_I}{\varepsilon_{le}}, \tag{3.2}$$

where A_I is the T-S amplitude at branch I of the instability. ε_{le}, the magnitude of the free-stream ζ_z-mode, is in contrast evaluated at the nose of the plate, where the receptivity mechanism is initiated. Therefore, C_I incorporates both the receptivity in the leading-edge region and the subsequent decay of the T-S wave upstream of the first neutral point; C_I is therefore sometimes labelled 'effective receptivity coefficient'. Note that, apart from the leading edge itself, the joint between the MSE leading edge and the flat plate – though rather smooth – also contributes to the receptivity (see e.g. Lin *et al.* 1992). The above definition of C_I enables us to compare our values with those reported in Wanderley & Corke (2001) for receptivity to free-stream sound at $F = 96$. A_I is obtained by matching a PSE solution for the development of the pure T-S wave to the amplitude of the boundary-layer disturbance from the present DNS (cf. figure 6*b*). The matched PSE data are used to trace the contribution of the T-S wave to the total disturbance back to branch I of the T-S mode. The values of C_I for the present vortical ζ_z-modes (spanwise free-stream vorticity) are compiled in table 2, where the coefficients for acoustic receptivity from Wanderley & Corke (2001) are also given. In Wanderley & Corke (2001), a leading edge with $AR = 20$ has been considered while there are no data for $AR = 6$. The receptivity coefficients found are lower by one order of magnitude than those reported in Wanderley & Corke (2001). In particular, the largest coefficient for vorticity is about 15 % of that for sound waves for both $F = 96$ and 56. Buter & Reed (1994) have observed as well that vortical receptivity is lower than that to acoustic waves. For a significantly higher frequency ($F = 230$) they have found that coefficients for receptivity to vortical modes are about 1/3 those for acoustic disturbances. The values in table 2 also indicate that receptivity to vortical modes with frequency $F = 96$ becomes about six times more efficient at the blunt leading edge than at the slender one, which holds for all three

AR	6				20			
F	56	96			56	96		
γ	0.1344	0.1008	0.1344	0.4032	0.1344	0.1008	0.1344	0.4032
$C_I^{vo} \times 10^3$	2.8	38.1	40.3	23.7	2.1	6.4	6.3	4.1
F					56		96	
$C_I^{ac} \times 10^3$					13.0		47.0	

TABLE 2. Receptivity to free-stream disturbances in terms of branch-I receptivity coefficients for T-S instability. Receptivity to spanwise vortical free-stream modes (C_I^{vo}) with different frequencies and vertical wavenumbers and to free-stream sound (C_I^{ac}, cf. Wanderley & Corke 2001).

values of γ considered. For $F = 56$, the receptivity is only 30 % larger in the case of the blunt leading edge.

4. Discussion and conclusions

Results from DNS of the receptivity and response of leading-edge flow to vortical free-stream disturbances are presented. The configuration considered incorporates aspects of flow around wings and blades, for instance the upstream stagnation point, the boundary-layer curvature and the streamwise pressure variations. Receptivity mechanisms, responsible for the transfer of energy from ambient perturbations to the boundary-layer instabilities, are a prerequisite of transition to turbulence. This highlights the relevance of receptivity studies, aiming to identify instabilities and their initial amplitudes, for a correct prediction of the transition location. DNS based on spectral methods has so far been successful in predicting receptivity of flow for relatively simple configurations such as flat plates (e.g. Schrader, Brandt & Henningson 2009), while more complex flows have been beyond the scope of these methods. With the introduction of the Spectral Element Method and the development of efficient algorithms, though, it is possible to carry out studies with spectral accuracy of receptivity to vortical modes for leading-edge flow. Previous investigations have shown that perturbation approaches for theoretical non-parallel receptivity prediction may prove inadequate (e.g. Collis & Lele 1999), and accurate simulations of the full geometry are therefore necessary.

The effect of leading-edge geometry is included in the present investigation by considering blunt and sharp elliptic noses with aspect ratios $AR = 6$ and 20, respectively. Simplified models for the vortical free-stream fluctuations are applied, which allow for setting two of the three vorticity components to zero. This enables us to single out the receptivity of the boundary layer to axial, vertical and spanwise free-stream vortices. A divergence-free inflow perturbation is obtained by putting the disturbance velocity parallel to the free-stream vorticity to zero. On approaching and passing the obstacle the disturbance field is distorted and displaced. This results in the forcing of velocity and vorticity in the components initially being zero.

Results can be summarized as follows. The boundary layer is most receptive to axial free-stream vortices with low and in particular with zero frequency, developing non-modal instability in the form of long streaks with strong streamwise disturbance velocity. It has been found here that the effect of leading-edge bluntness is insignificant in the presence of axial vortices – in line with asymptotic results by Goldstein & Leib

(1993) and Wundrow & Goldstein (2001). This is in contrast to the boundary-layer response to vertical free-stream vorticity. This type of perturbation is also able to excite non-modal instability, with amplitudes clearly exceeding that of the forcing. The key of the underlying receptivity mechanism is the conversion of wall-normal into streamwise vorticity through stretching and tilting of vertical vorticity at the leading edge, proposed before by Goldstein *et al.* (1992) and Goldstein & Wundrow (1998). This process is clearly stronger on the plate with blunt leading edge and for zero- and low-frequency vertical vorticities, as also predicted by Goldstein & Wundrow (1998). It is also found that leading-edge effects enhance receptivity to smaller spanwise scales. Free-stream modes with high frequency penetrate at the leading edge into the boundary layer to form non-modal disturbances with short streamwise scale. These disturbances suffer from rapid downstream decay in the shear region and do not attain amplitudes comparable to those of the low-frequency streaks.

The present findings on receptivity to streamwise and vertical free-stream vorticity are relevant to bypass transition due to free-stream turbulence. In flat-plate wind-tunnel experiments (e.g. Kendall 1985, 1998; Matsubara & Alfredsson 2001) streamwise elongated structures (Klebanoff modes) similar to the streaks found here have been identified as the prevalent feature of this transition scenario. Bypass transition has also been analysed numerically in Blasius flow (e.g. Brandt, Schlatter & Henningson 2004) and in flow around leading edges (Nagarajan, Lele & Ferziger 2007; Xiong & Lele 2007). The streaky structures observed in the experiments could be reproduced in these simulations; it was further shown that an increase of the integral turbulent length scale results in an upstream shift of the transition location. Indeed, the boundary layer is shown here to be most receptive to zero- and low-frequency vortical disturbances, a model for the long-wavelength components of natural free-stream turbulence.

T-S instability with rather low amplitudes is observed at high frequency. We have performed two-dimensional simulations with spanwise vortices in the free stream to compute branch-I receptivity coefficients for T-S waves. The efficiency of the receptivity mechanism to vortical modes has been found to be about 15 % of that to free-stream sound reported in the literature. Leading-edge bluntness significantly enhances receptivity for T-S instability, especially at higher frequencies. The T-S waves obtain their maximum amplitude rather far downstream and the level of disturbance remains small. In the present cases the T-S mechanism cannot compete with the non-modal low-frequency instability. We conclude that receptivity of leading-edge flow to high-frequency low-amplitude vortical free-stream modes is negligible in comparison to that to zero- or low-frequency disturbances.

It is interesting to note that bluntness effects are different when the leading-edge shape is parabolic instead of elliptic. While rarely used in wind-tunnel testing, parabolic cylinders have been popular in theoretical and numerical studies, as they are a good model of the leading-edge region of a thin airfoil and amenable to a convenient representation in parabolic coordinates. This configuration has streamline-shaped walls and therefore a favourable pressure gradient everywhere. Asymptotic results by Hammerton & Kerschen (1996, 1997) and numerical findings from Haddad & Corke (1998) reveal that an increase in nose radius decreases receptivity to sound, which is attributed to the damping effect of the increasing pressure drop on the T-S modes. The present results and those reported in the literature indicate the opposite behaviour for vortical and acoustic receptivities at elliptic leading edges: in this case an increase

in nose radius (bluntness) intensifies the region of adverse pressure gradient, which has a destabilizing influence on the evolution of T-S waves.

In summary, three mechanisms for receptivity to free-stream vorticity are relevant: axial vortices excite non-modal boundary-layer instabilities due to the lift-up mechanism; vertical vortices are subject to vortex stretching and tilting, creating streamwise vorticity followed by the lift-up mechanism; spanwise vortices trigger T-S instability through wavelength reduction of the upstream boundary-layer disturbance due to non-parallel effects at the leading edge.

The authors wish to acknowledge Dr Paul Fischer for providing the simulation code and Dr Ardeshir Hanifi for his support in the generation of the boundary conditions for the mean flow. David Tempelmann is acknowledged for providing data from PSE calculations. This research is funded by VR (The Swedish Research Council). Computer time provided by SNIC (Swedish National Infrastructure for Computing) at the National Supercomputer Centre, Linköpings Universitet, is gratefully acknowledged.

REFERENCES

Bertolotti, F. P. 1997 Response of the Blasius boundary layer to free-stream vorticity. *Phys. Fluids* **9** (8), 2286–2299.

Bertolotti, F. P. & Kendall, J. M. 1997 Response of the Blasius boundary layer to controlled free-stream vortices of axial form. *AIAA Paper* 97-2018.

Brandt, L., Schlatter, P. & Henningson, D. S. 2004 Transition in boundary layers subject to free-stream turbulence. *J. Fluid Mech.* **517**, 167–198.

Buter, T. A. & Reed, H. L. 1994 Boundary layer receptivity to free-stream vorticity. *Phys. Fluids* **6** (10), 3368–3379.

Choudhari, M. & Streett, C. L. 1992 A finite Reynolds number approach for the prediction of boundary layer receptivity in localized regions. *Phys. Fluids* A **4**, 2495–2514.

Collis, S. S. & Lele, S. K. 1999 Receptivity to surface roughness near a swept leading edge. *J. Fluid Mech.* **380**, 141–168.

Crouch, J. D. 1992 Localized receptivity of boundary layers. *Phys. Fluids* A **4** (7), 1408–1414.

Feng, H. & Mavriplis, C. 2002 Adaptive spectral element simulations of thin flame sheet deformation. *J. Sci. Comput.* **17** (1–3), 385–395.

Fischer, P., Kruse, J., Mullen, J., Tufo, H., Lottes, J. & Kerkemeier, S. 2008 *NEK5000 – Open Source Spectral Element CFD solver*. https://nek5000.mcs.anl.gov/index.php/MainPage.

Fischer, P. F. 1997 An overlapping Schwarz method for spectral element solution of the incompressible Navier–Stokes equations. *J. Comput. Phys.* **133**, 84–101.

Fischer, P. F. & Mullen, J. 2001 Filter-based stabilization of spectral element methods. *C. R. Acad. Sci. Paris* **332** (Série I), 265–270.

Fuciarelli, D., Reed, H. & Lyttle, I. 2000 Direct numerical simulation of leading-edge receptivity to sound. *AIAA J.* **38** (7), 1159–1165.

Goldstein, M. E. 1983 The evolution of Tollmien--Schlichting waves near a leading edge. *J. Fluid Mech.* **127**, 59–81.

Goldstein, M. E. & Hultgren, L. S. 1987 A note on the generation of Tollmien–Schlichting waves by sudden surface-curvature change. *J. Fluid Mech.* **181**, 519–525.

Goldstein, M. E. & Leib, S. J. 1993 Three-dimensional boundary-layer instability and separation induced by small-amplitude streamwise vorticity in the upstream flow. *J. Fluid Mech.* **246**, 21–41.

Goldstein, M. E., Leib, S. J. & Cowley, S. J. 1992 Distortion of a flat-plate boundary layer by free-stream vorticity normal to the plate. *J. Fluid Mech.* **237**, 231–260.

Goldstein, M. E., Sockol, P. M. & Sanz, J. 1983 The evolution of Tollmien–Schlichting waves near a leading edge. Part 2. Numerical determination of amplitudes. *J. Fluid Mech.* **129**, 443–453.

Goldstein, M. E. & Wundrow, D. W. 1998 On the environmental realizability of algebraically growing disturbances and their relation to Klebanoff modes. *Theoret. Comput. Fluid Dyn.* **10**, 171–186.

Haddad, O. M. & Corke, T. C. 1998 Boundary layer receptivity to free-stream sound on parabolic bodies. *J. Fluid Mech.* **368**, 1–26.

Hammerton, P. W. & Kerschen, E. J. 1996 Boundary-layer receptivity for a parabolic leading edge. *J. Fluid Mech.* **310**, 243–267.

Hammerton, P. W. & Kerschen, E. J. 1997 Boundary-layer receptivity for a parabolic leading edge. Part 2. The small-Strouhal-number limit. *J. Fluid Mech.* **353**, 205–220.

Hammerton, P. W. & Kerschen, E. J. 2005 Leading-edge receptivity for bodies with mean aerodynamic loading. *J. Fluid Mech.* **535**, 1–32.

Heinrich, R. A. & Kerschen, E. J. 1989 Leading-edge boundary-layer receptivity to free-stream disturbance structures. *Z. Angew. Math. Mech.* **69** (6), T596–T598.

Kendall, J. M. 1985 Experimental study of disturbances produced in a pre-transitional laminar boundary layer by weak free-stream turbulence. *AIAA Paper* 85-1695, pp. 1–10.

Kendall, J. M. 1998 Experiments on boundary-layer receptivity to free stream turbulence. *AIAA Paper* 98-0530.

Kerschen, E. J., Choudhari, M. & Heinrich, R. A. 1990 Generation of boundary layer instability waves by acoustic and vortical free-stream disturbances. In *Laminar-Turbulent Transition: Proceedings of the IUTAM Symposium*, Toulouse, France, pp. 477–488. Springer.

Lin, N., Reed, H. & Saric, W. 1992 Effect of leading edge geometry on boundary-layer receptivity to free stream sound. In *Instability, Transition and Turbulence* (ed. M. Hussaini, A. Kumar & C. Streett), pp. 421–440. Springer.

Maday, Y. & Patera, A. T. 1989 Spectral element methods for the Navier–Stokes equations. In *State of the Art Surveys in Computational Mechanics* (ed. A. K. Noor), pp. 71–143. ASME.

Maday, Y., Patera, A. T. & Ronquist, E. M. 1990 An operator-integration-factor splitting method for time-dependent problems: application to incompressible fluid flow. *J. Sci. Comput.* **5** (4), 310–337.

Matsubara, M. & Alfredsson, P. H. 2001 Disturbance growth in boundary layers subjected to free-stream turbulence. *J. Fluid Mech.* **430**, 149–168.

Nagarajan, S., Lele, S. K. & Ferziger, J. H. 2007 Leading-edge effects in bypass transition. *J. Fluid Mech.* **572**, 471–504.

Ohlsson, J., Schlatter, P., Mavriplis, C. & Henningson, D. S. 2009 The spectral-element and pseudo-spectral methods – a comparative study. In *ICOSAHOM 09*, Lecture Notes in Computational Science and Engineering. Springer, Trondheim Norway.

Patera, A. T. 1984 A spectral element method for fluid dynamics: laminar flow in a channel expansion. *J. Comput. Phys.* **54**, 468–488.

Rogler, H. L. & Reshotko, E. 1976 Spatially decaying array of vortices. *Phys. Fluids* **19** (12), 1843–1850.

Saric, W. S., Reed, H. L. & Kerschen, E. J. 2002 Boundary-layer receptivity to free stream disturbances. *Annu. Rev. Fluid Mech.* **34**, 291–319.

Schrader, L.-U. 2008 Receptivity of boundary layers under pressure gradient. *Tech. Rep.* TRITA-MEK 2008:08. Department of Mechanics, Royal Institute of Technology (KTH).

Schrader, L.-U., Brandt, L. & Henningson, D. S. 2009 Receptivity mechanisms in three-dimensional boundary-layer flows. *J. Fluid Mech.* **618**, 209–241.

Tufo, H. M. & Fischer, P. F. 1999 Terascale spectral element algorithms and implementations. In *Supercomputing, ACM/IEEE 1999 Conference*, Portland, OR.

Wanderley, J. B. V. & Corke, T. C. 2001 Boundary layer receptivity to free-stream sound on elliptic leading edges of flat plates. *J. Fluid Mech.* **429**, 1–21.

Wundrow, D. W. & Goldstein, M. E. 2001 Effect on a laminar boundary layer of small-amplitude streamwise vorticity in the upstream flow. *J. Fluid Mech.* **426**, 229–262.

Xiong, Z. & Lele, S. K. 2007 Stagnation-point flow under free-stream turbulence. *J. Fluid Mech.* **590**, 1–33.

Zaki, T. A. & Saha, S. 2009 On shear sheltering and the structure of vortical modes in single- and two-fluid boundary layers. *J. Fluid Mech.* **626**, 111–147.